Dust Emission And Star Formation Rate In High Redshift Weak Line Quasar

Yunhao Zhang,[1,2] Ran Wang,[1,2] Yali Shao,[1,2] Linhua Jiang,[1,2] and et at.

[1]Kavli Institute for Astronomy and Astrophysics, Peking University, Beijing 100871, China
[2]Department of Astronomy, Peking University, Beijing 100871, China

ABSTRACT

We present Herschel observations on 19 weak line quasars (WLQs) by Spectral and Photometric Image Receiver (SPIRE). This WLQ sample is selected from Sloan Digital Sky Survey (SDSS) with reliable redshift measurements at $2 < z < 5$ and weak line featured spectrum. Far Infrared (FIR) Spectral Energy Distribution (SED) of WLQs with all FIR luminosity over $10^{12} L_\odot$ shows strong star formation heated dust emission. Star formation rates (SFRs) of WLQs in the range of $300-3000 M_\odot/yr$ are significantly higher than that of radio quiet normal quasar comparison sample on average, which is selected from SDSS Data Release 14 (DR14) quasar catalog within comparable luminosity and redshift range. In addition, extremely massive dust content with an average dust mass of $10^9 M_\odot$ and relatively lower dust temperature also indicates a abundant cold gas and dust environment in host galaxy. Through the multiwavelength analysis of WLQs, we have deep insights into the evolution stage of WLQ host galaxies and eventually identify this kind of objects as early stage of post merger quasar-starburst system. Under this assumption, physical origin of weak emission line features is interpreted by anemic Broad Emission Line Region (BELR) scenario and other properties like weak X-ray luminosity could also be partly understood by this hypothesis. Further observation is also required to provide more evidence on this young type quasar hypothesis to reveal more in origin of WLQs and co-evolution of Active Galactic Nuclear (AGN) and host galaxy.

Keywords: Active—Galaxies: ULG—QSO: Extra Galactic

1. INTRODUCTION

Strong ultraviolet (UV) and optical radiation from Broad Emission Line Region (BLER) is one prominent signature of active galaxy nuclei (AGN). However, one population of about 100 Sloan Digital Sky Survey (SDSS) quasars has been found to show features of weak broad emission line and almost missing narrow emission line (Anderson et al. 2001; Collinge et al. 2005; Diamond-Stanic et al. 2009; Plotkin et al. 2010; Hryniewicz et al. 2010; Meusinger&Balafkan 2014), which has been subsequently categorized in to a new branch called weak line quasars (WLQs). In addition, another kind of intrinsically X-Ray weak quasars shows similar weak line features spectroscopy to WLQs which is also added to WLQs afterwards. One of the best studied case is the radio quiet quasar PHL 1811 (Leighly et al. 2007a; 2007b). Analysis on the X-ray

Corresponding author: Yunhao Zhang
zhangyunhao@pku.edu.cn

data from Chandra observation suggests that super Eddington accretion rate might account for the extremely weak luminosity. Further multi wavelength study on this object also indicates that there is no forbidden and semi-forbidden line emission and strong blue shifted low Equivalent Width (EW) high ionization rest frame UV emission line, implying a strong radiatively driven wind dominated BELR.

Since the discovering of WLQs, it has been puzzling what accounts for the lack of strong emission line in quasar spectrum which could not be predicted by AGN unified model. WLQs tend to be so luminous that can't be explained by a radiatively inefficient accretion flow as has been called Optically Dull AGN (Nicastro et al. 2003; Hawkins et al. 2004; Tran et al. 2011; Trump et al. 2011). Also there is no evidence that WLQs are affected by gravitational lensing (Shemmer et al. 2006; 2009). At first, WLQs were considered to belong to BL Lacertae objects, whose ultraviolet (UV), optical and infrared (IR) continuum will be realistically boosted by radiation from radio jet on line of sight, causing the line emission to be masked by the enhanced continuum.

Nevertheless, broad band Spectral Energy Distribution (SED) and spectroscopic observations of WLQs both indicate that there is no significant difference between the continuum emission in UV - optical - Mid Infrared (MIR) of WLQs and that of normal quasars (Lane et al. 2011; Jianfeng Wu et al. 2012). In fact, the majorities of WLQs are radio quiet (Collinge et al. 2005; Shemmer et al. 2009; Plotkin et al. 2010) and moreover there is no obvious optical variation and polarization (Fan et al. 1999; Smith et al. 2007; Shemmer 2009; Heidt Nilsson et al. 2011), all of which manifest no evidence of the orientation effect of radio jet. Apart from these, there are considerable WLQs with extremely weak X-Ray luminosity(Shemmer et al. 2009; Plotkin et al. 2010; Jianfeng Wu et al. 2011; 2012), making it to be inconsistent with BL Lacertae scenario and leaving more conundrums to understand the origin of WLQs at the same time. Thus WLQs tend to represent some unclear extreme physics driven by quasar intrinsic properties instead of some orientation effects.

On the other hand, according to the universal relationships between SMBH and its host galaxy (Kormendy & Richstone 1995; Magorrian et al. 1998; Ferrarese & Merritt 2000; Gebhardt et al. 2000; Tremaine et al. 2002), their formation process are tightly correlated (Marconi Hunt et al. 2003). Signatures of star formation like strong Far Infrared (FIR) dust continuum or molecular CO line emission has been searched at millimeter wavelengths with samples of quasars at $2 < z < 6$ to study the SMBH-galaxy co-evolution (Omont et al. 1996; Bertoldi et al. 2003). The millimeter observation show a curious trend that those quasars detected in the millimeter tend to have weak UV emission lines than the millimeter non-detected sources (Omont et al. 1996; Bertoldi et al. 2003; Wang et al. 2008; Willott et al. 2010). These results suggest an early phase of quasar-galaxy evolution, in which the central AGN has just turned on, the line emitting regions have not been fully formed, and active bulge building via star formation is still ongoing in the quasar host galaxy. To test the hypothesis that WLQs are early type quasar system and understand the SMBH-galaxy formation in the early universe, a systematic study of star formation activity in the host galaxy of the sample of WLQs is required.

Here it is the first time that Herschel SPIRE photometry observation is applied on WLQs and 19 targets has selected from WLQ catalog in previous literature. In section 2 we describe our WLQ sample selection and multi wavelength properties. Herschel observation and subsequent data analysis are described in Section 3, and we present our results in Section 4. For the discussion and conclusion, we will present in Section 5. Through-

out, we adopt $H_0 = 70 km s^{-1} Mpc^{-1}, \Omega_\Lambda = 0.7, \Omega_m = 0.3$. We define radio quiet quasars as having radio loudness parameter $R < 10$, and error bars are reported at the 68% confidence level, unless otherwise.

2. WLQ SAMPLE PROPERTIES
2.1. *Sample Selection*

Samples of WLQs at $2 < z < 5$ are collected from the literature (Collge et al. 2005; Plotkin et al. 2010; Diamond-Stanic et al. 2009; Shemmer et al. 2009). Then several criteria are applied to our sample selection: Firstly, WLQ objects have reliable redshift estimate from SDSS spectrum. Secondly, WLQ objects do not have strong radio emission in order to make sure that the weak line feature is not due to relativistically boosted continuum. Thirdly, WLQ objects do not have damped Lyα absorption in the UV spectra in order to ensure that the weak line feature can not be caused by absorption. We then simulate FIR flux density according to an FIR-AGN luminosity relation from high redshift quasar-star burst system (Wang et al. 2011). Finally, we select a sample of 19 objects which have estimated flux density over 21 mJy at $250 \mu m$ or $350 \mu m$. So that sources can be detected at over 3σ by SPIRE in 15 minutes of observing time under small map mode if FIR emission is powered by star forming activity and in addition, we also expect to detect the brightest targets at about 3σ at $500 \mu m$.

2.2. *UV-Optical-IR SED*

All of our WLQ sample targets have reliable redshift estimate from SDSS spectrum (Schneider et al. 2010; Paris et al. 2012; 2018) so that we could acquire accurate rest frame UV-optical-IR SED for each individual WLQ based on all sky survey archive data from SDSS, 2-Micron All Sky Survey (2MASS; Skrutskie et al. 2006), United Kingdom Infrared Telescope (UKIRT) Infrared Deep Sky Surveys (UKIDSS; Lawrence et al. 2007) and Wide field Infrared Survey Explorer (WISE; Wright et al. 2010). As has been stated in (Lane et al. 2011; Jianfeng Wu et al. 2012), there is no significant discrepancy between broad band SED of WLQs and that of normal radio quiet quasar. After applying minimum Chi-Square fitting to SDSS data with average quasar template (Elvis et al. 1994; Richards et al. 2006; Shang et al. 2011), bolometric luminosity can be estimated by template monochromatic luminosity at $5100 \mathring{A}$ with a empirical bolometric correction (Richard et al. 2006). In addition, there are 11 targets among WLQ sample with Black Hole mass measurements based on Black Hole mass estimators like Hα, MgII and CIV (Yue Shen et al. 2011; Nikolajuk et at. 2011; Shemmer et at. 2010; 2015)
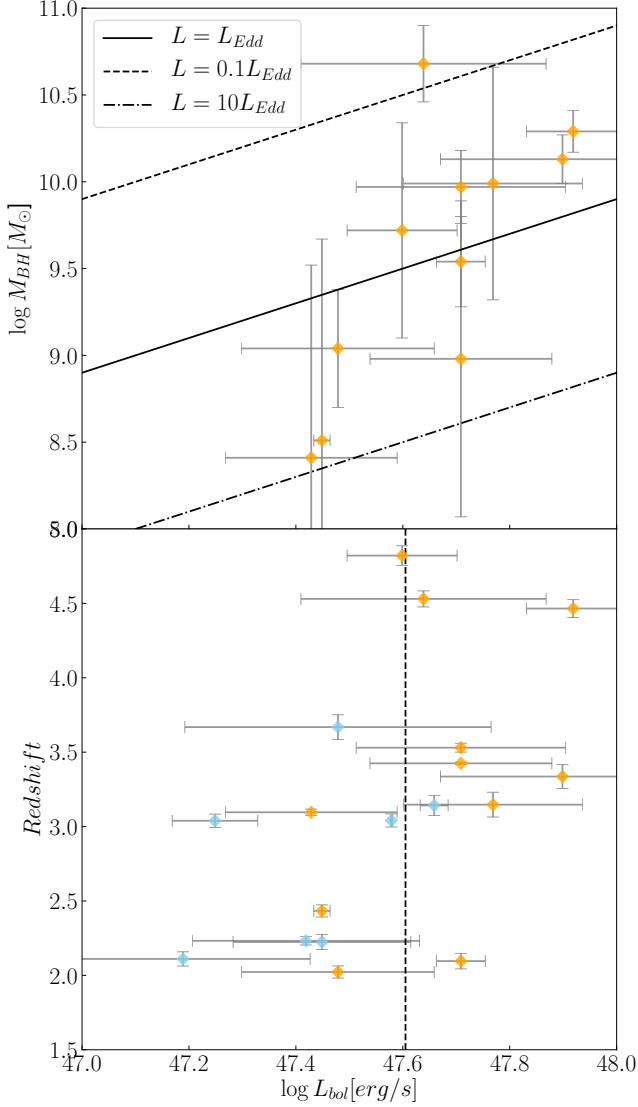
Figure 1. Upper panel shows the distribution of bolometric luminosity and blackhole sass in WLQs. Bolometric luminosity is calculated from monochromatic luminosity at $5100\mathring{A}$ from optimize fitting quasar template (Elvis et al. 1994) and blackhole mass is measured based on the continuum luminosity and Full Width Half Maximum (FWHM) of emission line estimators (Shen et al. 2011). Solid line represents the Eddington limit accretion. And upper dashed line and lower dashed dot line represent $\frac{L_{bol}}{L_{Edd}} = 0.1$ and 10 separately. The lower panel shows distribution of redshift and luminosity, among which blue points represent targets without blackhole mass measurements and red points represent targets with blackhole mass. The vertical dashed line is mean bolometric luminosity of whole WLQ sample.

from the data in previous literature and archive. Although incomplete and with large scatter, targets with blackhole mass measurements have a wide redshift range and these estimations are robust enough to manifest
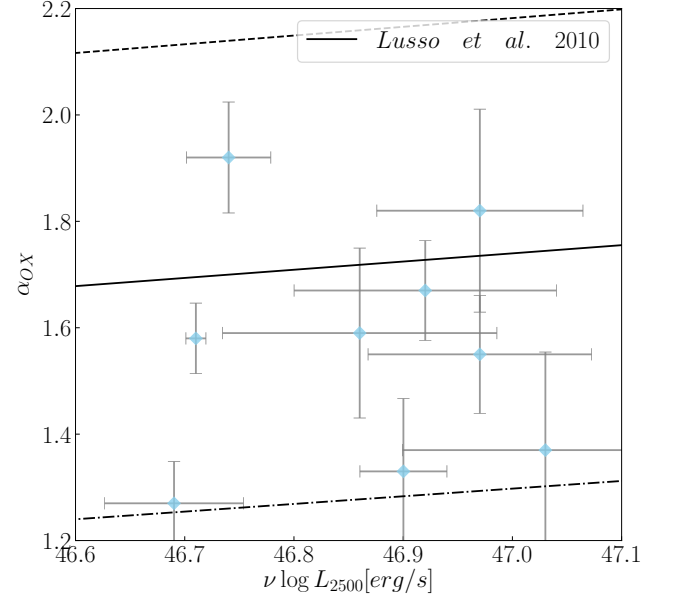

Figure 2. The distribution of optical-X ray ratio α_{OX} and monotonous luminosity at $2500\mathring{A}$ in WLQs. Monotonous luminosity $L_{2500\mathring{A}}$ is estimated from the best fitting quasar average template and optical-X ray ratio α_{OX} based on SDSS photometry and soft x-ray flux density. The former is also calculated from quasar template fitted by SDSS photometry data and later is measured from Chandra soft X-ray band count rate by assuming a power law spectrum with photon index of 2. The solid line is empirical quasar $\alpha_{OX} - L_{2500\mathring{A}}$ relation (Lusso et al. 2010). The upper dashed line and lower dashed dot line both represent the scatter of the empirical relation.

properties of the whole sample. As showed in Figure 1, our WLQ targets have a mean bolometric luminosity of $10^{47.6} erg/s$ and the accretion rate distribution is close to the Eddington limit, indicating that our sample is an luminous and high accretion rate WLQ sample with high mean blackhole mass of $10^{9.6} M_{\odot}$. Eventually, UV-optical properties will be listed in Table 1 and NIR-MIR SED will be listed in Table 2.

2.3. X-Ray Radiation

There are 9 targets of our WLQ sample with Chandra X-ray observation obtained from previous literature or data archive, which is over the half of total number of our WLQ sample, enabling us to know about the properties of X-ray radiation of our WLQ sample (Nikolajuk et al. 2011; Jianfeng Wu et al. 2012; Bin Luo et al. 2015; Shemmer et al. 2009). Here the X-ray to optical ratio α_{OX} is defined by the equation as follow

$$\alpha_{OX} = -\frac{log(f_{2keV}/f_{2500\mathring{A}})}{log(\nu_{2keV}/\nu_{2500\mathring{A}})}$$

Among the equation above, X-ray flux density is estimated from the soft x-ray band (0.5-2keV) count rate by assuming a power law spectrum with photon index of 2. And rest frame monotonous UV flux density at $2500\mathring{A}$ is obtained from the best fitting quasar template. We use this ratio to be an indicator of the strength of X-ray radiation related to its UV luminosity, indicating that the greater the α_{OX} is, the weaker the X-ray is when compared with UV luminosity. In addition, it has been stated that there is a inverse relation between X-ray luminosity and UV luminosity, causing the ratio α_{OX} to increase as UV luminosity increase (Stocke J.T. et at. 1991; Wilkes B.T. et al. 1994; Green P.J. et al.

1995, Lusso et at. 2010; 2018). Thus we will check the $\alpha_{OX} - L_{2500}$ distribution of our WLQ sample to learn about their X-ray radiation properties. As is showed in Figure 2, there are only 2 targets with relatively high α_{OX} when compared with an $\alpha_{OX} - L_{2500\mathring{A}}$ relation from literature. As is discussed in previous work (Leighly et al. 2006, 2007; Jianfeng Wu et al. 2012; Bin Luo et al. 2015), WLQ are divided into two categories, X-ray weak and X-ray normal, according to the activity of their X-ray radiation when compared with normal quasars. It indicates that the majorities of our WLQ sample are X-ray normal ones although there are some X-ray weak targets, and all the data will be listed in Table 3.

Table 1. UV-Optical Properties

SDSS Name J2000	Redshift[a]	u[b] μJy	g[b] μJy	r[b] μJy	i[b] μJy	z[b] μJy	$\log L_{bol}$[c] erg/s	$\log M_{BH}$[d] $M_\odot$
031712.23-075850.3	2.22	60±2.3	86±0.8	107±2	125±2	145±9	47.45	...
082722.73+032755.9	2.02	104±3	128±2	165±2	208±2	225±7	47.48	9.04±0.34
083122.57+404623.3	4.82	0.076±0.017	18±0.36	27±1.1	86±2.0	106±5	47.59	9.7±0.62
092832.88+184824.4	3.13	0.705±0.436	123±1	319±2	394±3	468±5	48.16	...
095041.07+233159.5	2.11	57.8±1.8	71.7±1.5	85.9±1.3	77.4±1.3	79.5±1.4	47.18	...
103601.11+084948.4	3.66	7.34±0.97	25.1±0.6	55.3±1.1	56.5±1.3	72.2±4.1	47.47	...
113747.64+391941.5	2.43	39.7±1.3	59.8±1.2	98.7±2.3	121±2	131±4	47.44	8.51±1.16
114412.76+315800.8	3.33	2.61±1.02	82.2±1.9	136±2	170±3	188±5	47.89	10.13±0.14
123132.37+013813.9	3.14	3.61±1.4	97.6±1.9	89.9±2	413±3	150±5	47.76	9.99±0.67
123743.08+630144.8	3.42	1.16±1.01	34.3±0.9	87.4±1.9	111±2	137±5	47.7	8.98±0.91
132809.59+545452.7	2.09	185±5	243±9	268±4	272±4	288±5	47.7	9.54±0.26
133219.65+622715.9	3.14	11.9±1.4	56.4±1.6	77±1.1	99.8±2	98.4±8	47.65	...
142505.59+035336.2	2.23	59.1±2	87.4±0.7	126±1	141±3	149±4	47.41	...
144803.36+240704.2	3.53	0.121±0.063	37.5±0.7	77.1±1.1	88.6±1.1	107±4	47.7	9.97±0.21
150739.66-010911.0	3.03	0.297±0.202	15.5±0.5	29.6±0.8	48.4±1.3	68.4±3.7	47.24	...
155203.30+352440.3	3.04	3.12±1.03	46.8±0.9	74.8±1.4	98±3	120±4	47.57	...
155645.30+380752.8	3.09	83.9±1.2	32.2±1.1	54.8±1.2	68±1.9	73.1±4.4	47.42	8.41±1.11
160336.64+350824.2	4.46	1.22±0.762	15.2±0.4	55.4±2	139±2	167±4	47.91	10.29±0.12
163411.81+215325.0	4.53	0.607±0.603	5.71±0.36	27.7±0.6	89±1.4	112±4	47.63	10.68±0.22

[a] Redshift is obtained from SDSS DR14 catalog estimated by SDSS spectrum

[b] Flux density at u, g, r, i, z is calculated from PSF magnitude in SDSS DR14 catalog. Galactic extinction is also corrected with empirical dust extinction law

[c] Bolometric luminosity is estimated based on monochromatic luminosity at $5100\mathring{A}$ from optimize fitting quasar template Richard et al. 2006

[d] Blackhole mass is estimated from several indicators based on Shen et al. 2011

Table 2. NIR-MIR SED

SDSS Name J2000	J[a] μJy	H[a] μJy	K[a] μJy	3.35μm[b] μJy	4.61μm[b] μJy	11.6μm[b] μJy	22.1μm[b] μJy
031712.23-075850.3	...	272±65	...	111±8	132±25	437±126	1840±910
082722.73+032755.9	159±5	168±6	153±6	139±9	274±20	1350±180	4530±520
083122.57+404623.3	...	209±52	...	50.0±6.8	65±13.7	335±115	1960±860
092832.88+184824.4	484±34	475±46	507±51	424±12	381±16	1160±160	3970±1010
095041.07+233159.5	...	...	...	55±7.7	110±15	385±130	3860±740
103601.11+084948.4	72.3±2.8	52.7±5.9	84.6±5.8	41±15	36.1±12	313±134	2190±1100
113747.64+391941.5	...	...	...	106±7	90.1±13.4	447±108	2220±970
114412.76+315800.8	186.0±49.0	...	...	149±9	186.0±14	1010±110	2100±890
123132.37+013813.9	155±4	137±4	136±5	97.6±7.6	89.9±14.6	413±129	3190±1020
123743.08+630144.8	...	...	...	125±6.2	117± 17	687±87	2420±680
132809.59+545452.7	...	251±67	353±67	259±8	435±14	2110±110	5740±790
133219.65+622715.9	...	...	...	75.4±4.8	83.6±8	214±67	1160±580
142505.59+035336.2	132±6	142±7	142±8	...	...	...	...
144803.36+240704.2	...	...	...	76.9±4.3	80.3±7.7	258±61	1640±630
150739.66-010911.0	84.2±5.4	96.2±6	103±7	109±6	150±11	1050±110	4040±740
155203.30+352440.3	193±57	...	...	137±6	172±9	676±64	1320±560
155645.30+380752.8	128±45	...	...	61.5±4.1	67±7.6	406±59	1560±550
160336.64+350824.2	166±47	...	...	239±7	191±9	711±54	2430±470
163411.81+215325.0	...	...	...	208±9	157±13	473±101	2980±800

[a] J, H, K flux density is obtained from UKIDSS if targets are in UKIDSS catalog, otherwise 2MASS flux density will be used

[b] 3.35μm, 4.61μm , 11.6μm, 22.1μm are flux density at four bands from WISE all sky catalog

Table 3. X Ray Radiation

SDSS Name J2000	Count Rate[a] $10^{-3} counts/s$	f_ν[b] $10^{-3}\mu Jy$	$log\nu L_{2keV}$[b] erg/s	$log\nu L_{2500\mathring{A}}$[c] erg/s	α_{OX}[d] ...
031712.23-075850.3	5.41±1.25	12.19	44.93	46.71	1.58
082722.73+032755.9	<0.97	<1.68	<44.16	46.74	>1.92
083122.57+404623.3	13.13±1.91	37.03	45.64	46.86	1.59
123132.37+013813.9	20.44±2.38	47.94	45.9	47.03	1.37
123743.08+630144.8	<3.3	<10.88	<45.1	46.97	>1.55
132809.59+545452.7	3.12±1.52	4.89	44.75	46.97	1.82
133219.65+622715.9	2.15±1.27	3.63	45.181	46.92	1.67
155645.30+380752.8	10.16±2.06	23.85	45.617	46.69	1.27

Table 3 continued

Table 3 *(continued)*

SDSS Name	Count Rate[a]	f_ν[b]	$log\nu L_{2keV}$[b]	$log\nu L_{2500\mathring{A}}$[c]	α_{OX}[d]
J2000	$10^{-3}counts/s$	$10^{-3}\mu Jy$	erg/s	erg/s	...
163411.81+215325.0	3.9±1.19	11.02	46.04	46.9	1.33

[a]Chandra soft X-ray band 0.5-2keV count rate

[b]Flux density and luminosity at 2keV is calculated by assuming a power law spectrum with photon index $\Gamma = 2$

[c]Monochromatic luminosity at $2500\mathring{A}$ is estimated from optimize fitting quasar template Richard et al. 2006

[d]α_{OX} is calculated based on previous defined equation

2.4. *Radio Continuum*

All of our WLQ samples are in FIRST footprint, 4 targets among which have FIRST 1.4GHz flux detection and other non detection targets are measured with 3σ upper limit. Then radio loudness is defined as follow:

$$R = \frac{f_{5GHz}}{f_{4400\mathring{A}}}$$

Among this equation, f_{5GHz} is obtained from FIRST flux density by assuming a flat power law radio continuum with spectral index of zero. And $f_{4400\mathring{A}}$ is from the average quasar SED template. Then all the results are listed in Table 4. Among FIRST detection sources, three of them is defined as radio loud quasar, whose radio loudness are over 10. In order to exclude the components of radio continuum on dust emission and also avoid strong radio emission which could be caused by radio jet, we remove radio continuum contribution to FIR emission by subtracting model Point Spread Function (PSF) when estimating SFR. However, when we do stacking analysis, we exclude all these targets in order to avoid sample bias of BL Lacerate objects whose weak line feature is cause by relativistically boosted continuum of jet component. And for the other non detection WLQ sources, all the upper limit of radio loudness are lower than 15 which is enough to consider all these targets as radio quiet WLQ sample without jet component contribution. SFRs of these targets will be estimated directly from observed flux which will be introduced in next Section.

3. OBSERVATION AND DATA ANALYSIS

3.1. *Herschel Observation*

The SPIRE bolometer camera on Herschel at $250\mu m$, $350\mu m$ and $500\mu m$ measures with high sensitivity the rest frame 40 to $170\mu m$ emission at $2 < z < 5$, where the peak of $30K$ to $60K$ thermal dust emission heated by star formation in high redshift galaxies. We adopted the SPIRE small map mode with 5 repetition for all the targets. Observing time for each of the 19 targets is about 901 seconds in order to get over 3σ detection for all 19 targets at $250\mu m$ or $350\mu m$ when considering the instrument noise in small map mode and SPIRE confusion limit. The observing time for each object includes 185 seconds of on-source integration time, 536 seconds of instrument and observation overheads, and 180 seconds observatory overheads, which results in 4.8 hours observing time in total, including all the overheads. In addition, we have checked our AORs with the Herschel Duplication Checker and the Herschel Reserved Observations Search Tool. Only one of our target, SDSS J123743.08+630144.9, is spatially overlapped with an existing OT1 SPIRE photometer program. Nevertheless, the observing time of the existing program at the overlapping area is only 169 seconds, which can not reach the required sensitivity for our scientific goal. Thus we keep this object in our observation and adopted 901 seconds observing time.

3.2. *Comparison Sample Selection*

In order to learn about the relative strength of WLQ dust emission and star formation activity, we need to compare our WLQ sample with radio quiet quasars with normal emission line features. A nearly complete normal quasar catalog from SDSS Data Release 14 (DR14) is selected for comparable analysis (Paris et al. 2018). These quasars all have well identified redshift from SDSS spectra and well measured u, g, r, i, z band photometry data. We inspect the radio properties of these quasars in order to avoid radio continuum contribution to dust emission. All the sources not in FIRST footprint are excluded and for the other candidates, we only select non 3σ FIRST detection sources so that these final ra-
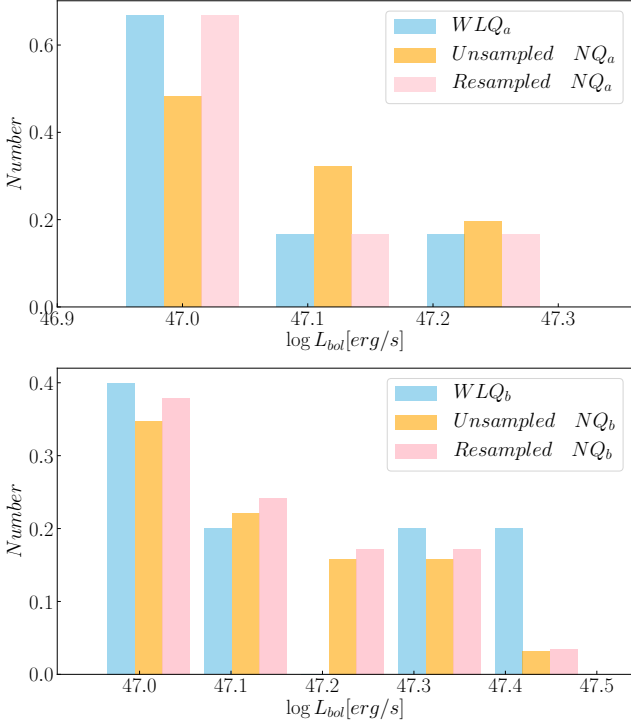
Figure 3. Normalized bolometric luminosity distribution of WLQ targets and normal quasar comparison samples. Left panel shows the number distribution of comparison sample a and the right panel shows that of control sample b. The cyan bar show the histogram of WLQ bolometric luminosity. The orange bar represent the histogram of normal quasar comparison which is directly selected from SDSS catalog and inspected with Herschel archive data coverage but without sampling. Re-sampled comparison sample is showed in green bars to follow similar distribution with that of weak WLQs.

dio quiet sample will be prevented from the effect of radio component. Next, we only preserve the sources with Herschel SPIRE image data coverage. Here we use Python web programming to search for all images with our sources observed from Herschel High Level Image (HHLI) in NASA/IPAC Infrared Science Archive (IRAC). It will expand our comparison sample size for further high quality stacking analysis because our SDSS sources have a wide spatial distribution, some of which are not in Herschel large area sky survey footprint like Herschel Stripe 82 Survey (HerS) and Herschel Multi-tiered Extragalactic Survey (HerMES). Thus, we should be careful with these image data to avoid the sample selection bias to luminous infrared sources by inspecting observing tag. And visual inspection is also applied to check the quality of the image data to exclude out targets near the edge of field of view. Eventually, a nearly complete no bias catalog of normal radio quiet quasars is obtained for further stacking analysis.

In addition, these radio quiet normal quasars with high quality SPIRE image data will be divided into several subsamples according to our WLQ sample redshift distribution. As has been stated in Section 2.4, after having excluded 3 FIRST detection radio loud WLQ targets, there are 6 WLQ sources in $2 < z < 2.5$ and 5 WLQ targets in $3 < z < 3.5$. Apart from that, there are 2 WLQ targets with redshift at 3.53 and 3.60 and three targets with redshifts higher than 4, which is added to another WLQ subsample. In order, we named them as WLQ_a, WLQ_b and WLQ_c. And then our comparison sample will be generated with similar luminosity and redshift range to these two WLQ subsamples. However, because of wide redshift range of WLQ_c, it is not proper for a robust comparison but we will still discuss about them in later analysis. And then for WLQ_a and WLQ_b, we get 342 normal quasar sources in $2 < z < 2.5$ and 95 sources in $3 < z < 3.5$. Nevertheless, it is still not perfect if we just set comparison sample to have similar luminosity and redshift range. Considering that the luminosity distribution of our WLQ targets is quiet different from that of normal quasar because of the limitation of WLQ subsample size. So that it necessary for us to resampling the comparison sample to make the luminosity distribution follow the trend of WLQ targets. We divide these sources into two directory according to their luminosity and then adjust the fraction of high luminosity part or low luminosity part in the principle of keeping more comparison sample as much as possible. Eventually we get 247 sources in $2 < z < 2.5$ and 87 sources in $3 < z < 3.5$. In convenient, we name these two sample as NQ_a and NQ_b separately. The luminosity distribution of WLQ subsample and control sample in two redshift ranges is showed in Figure 3.

3.3. *Stacking Analysis*

Although we hope to know FIR SED of each individual quasar , the detection sensitivity limit us to have over 3σ detection for each single target. However, stacking analysis provide us a way to get the average median SED of our control sample. The noise of each single Herschel image is often so strong to prevent us to get high sensitivity flux photometry. Nevertheless, after multi image stacking we could low down pixel to pixel RMS and finally estimate the average flux density with high Signal-to-Noise Ratio (SNR). Before stacking, a fixed size subimage should be cut out first from Herschel image data for each normal quasar and then all the images in the same SPIRE band of control sample will be combined. When combining images of different targets, boot strapping method is applied to calculate the median and 1σ standard deviation in each pixel. Through this way,
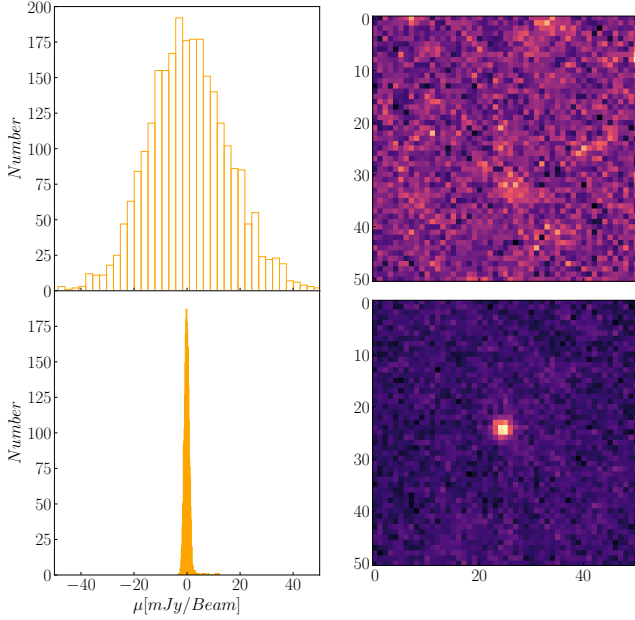
Figure 4. The stacking analysis is applied to low down the SPIRE image noise level. Upper and lower right panel show the single exposure SPIRE image of one comparison target and multi stacking image of control sample 1. Upper and lower left panel show the distribution of the pixel value for the single exposure SPIRE image of one comparison target and multi stacking SPIRE image of control sample 1.

we could avoid bias to high luminosity end of the comparison sample and RMS of stacking image could also be lowed down by iteration of resampling control sample. In addition, the instrument noise and statistic dispersion are both include in our standard deviation calculation. After that, all the median pixels constitute the stacking image and the 1σ standard deviation make up the error map. As is showed in Figure 4, the RMS is highly decreased by stacking analysis to about 0.5-1.0 mJy which is much smaller than that of single image.

3.4. SPIRE Photometry

We use the Herschel Interactive Processing Environment (HIPE) to do the photometric data reduction. As calibrated products from the Standard Pipeline applied, final flux density is measured by program "sourceExtractorSussextractor" in HIPE and then 1σ Root Mean Square (RMS) is estimated from the pixel to pixel standard deviation of the residual map after subtracting each individual point source with model SPIRE PSF. In this way, instrument noise in small map mode and SPIRE confusion limit will all be all included into our error estimate. Eventually it results the 1σ noise level to be

7.54mJy, 7.21mJy, 8.28mJy of WLQ targets separately at $250\mu m$, $350\mu m$ and $500\mu m$ SPIRE band . Under this noise level, there are 16 targets with both over 3σ detection in at least two SPIRE bands, among which 13 targets have over 3σ detection at all three bands. And only one of the remaining 3 targets don't have over 3σ detection in any SPIRE band. And the flux density of each target is presented in Table 4, where 3σ upper limit is showed when there is no detection. In addition, we will also apply our photometry to our stacking SPIRE image, which will be discussed in Section 3.3 and 3.4 in detail.

3.5. Dust Emission and SFR

As is presented in Section 3.2, rest frame FIR SED is obtained from high sensitivity small map mode SPIRE photometry observation and nearly all the targets have high quality flux measurement at all SPIRE bands which is showed in Table 4. Before SFR measurement, we should subtract the contribution from radio continuum, which will include bias to our SFR measurements. There are three targets with VLA FIRST detection so we should care for them. Radio component flux at all three SPIRE band is calculated based on a flat radio continuum by assuming the spectral index as zero. Next, a model PSF is subtracted from the original SPIRE image and the photometry will be redone with the same procedure as discussed in Section 3.2. After subtraction, a empirical modified gray body dust model fitting is applied to each individual source by assuming an emissivity as 1.6 (Beelen et al. 2006). Under this condition, dust temperature and scale is set as two free parameter. We adopt Python CurveFit program to estimate the optimize parameter and 1σ confidence level. We integrate the dust model during rest frame $8\mu m \sim 1000\mu m$ wavelength range to get the far infrared luminosity based on the optimize fitting parameter. Here, we assume a star formation contribution fraction as 0.5 for all the targets in order to exclude the AGN heated dust emission and eventually SFR is estimated by the Kennicutt Schmidt FIR luminosity-SFR relation and dust mass is calculated based on Berta et al. 2016 by assuming an empirical opacity. All the results are showed in Table 5 and all the 1σ error is estimated by 1σ standard deviation of Monte Carlo Method Simulation results. Till now, we have studied on all multi wavelength properties from X-ray to radio of our WLQ targets and each multi wavelength SED will be showed in Figure 5, including stacking SED of our control sample.

Table 4. SPIRE Photometry Measurement

SDSS Name	S_{250}[a]	S_{350}[a]	S_{500}[a]	f_{VLA}[b]	R[c]
J2000		mJy	mJy	mJy	mJy
031712.23-075850.3	24.49 ±10.23	<31.16	26.58±10.38	< 0.86	7.0
082722.73+032755.9	20.53±7.56	<22.1	<24.27	< 0.41	2.4
083122.57+404623.3	12.01±7.67	<21.63	<24.86	<0.42	<15.6
092832.88+184824.4	30.51±7.13	48.33±6.58	32.25±7.64	9.21±0.16	33.1
095041.07+233159.5	53.51±7.16	38.54±7.09	26.36±7.58	<0.48	<6.2
103601.11+084948.4	<20.93	<19.34	<23.97	<0.65	<16.6
113747.64+391941.5	35.15±8.17	32.94±7.61	21.59±8.66	<0.41	<4.2
114412.76+315800.8	38.57±7.15	38.02±6.46	31.3±7.41	<0.71	<5.5
123132.37+013813.9	20.28±7.3	21.76±7.2	24.1±7.45	12.56±0.43	73.7
123743.08+630144.8	31.99±7.15	27.55±7.22	<24.87	<0.44	<5.6
132809.59+545452.7	66.95±7.54	69.56±6.76	53.33±7.3	<0.45	<1.7
133219.65+622715.9	25.9±6.84	36.93±6.38	25.22±7.28	3.62 ± 0.13	42.3
142505.59+035336.2	38.1±7.4	40.06±6.8	33.12±8.3	<0.46	<4.25
144803.36+240704.2	<21.94	9.86±7.1	13.11±8.33	<0.43	<5.9
150739.66-010911.0	38.25±7.73	53.6±7.53	60.89±8.11	<0.42	<11.6
155203.30+352440.3	21.87±8.37	33.84±7.82	34.26±9.91	<0.42	<5.4
155645.30+380752.8	56.92±7.72	54.94±7.57	23.03±9.01	<0.39	<7.4
160336.64+350824.2	49.91±7.95	57.52±7.5	42.7±8.77	<0.4	<5.9
163411.81+215325.0	13.78±8.39	23.53±7.9	23.22±9.19	<0.4	<11.7
Normal Quasar a	11.20±0.79	9.04±0.79	5.42±0.98	...	...
Normal Quasar b	10.85±1.26	9.39±1.39	5.51±1.79	...	...

[a] SPIRE observational flux density at $250\mu m$, $350\mu m$, $500\mu m$ is measured and their 1σ RMS

[b] Flux density in FIRST is estimated from point source photometry on VLA image

[c] Radio loudness is estimated by the rest frame monochromatic flux density at $4400\mathring{A}$ and radio flux density at 5 GHz

Table 5. Dust Emission and Star Formation Activity

SDSS Name	T_{dust}[a]	$logL_{FIR}$[b]	SFR[c]	M_{Dust}[d]
J2000	K	erg/s	$M_\odot/yr$	$M_\odot$
031712.23-075850.3	29.18±6.54	46.03±0.47	242.8±207.1	9.36±0.50
082722.73+032755.9	32.74±9.35	45.86±0.47	166.7±156.4	8.92±0.46
083122.57+404623.3	47.75±12.95	46.58±0.47	860.8±862.6	8.71±0.42
092832.88+184824.4	36.38±4.60	46.47±0.37	674.3±386.2	9.27±0.33
095041.07+233159.5	39.84±5.63	46.40±0.36	576.5±308.5	8.98±0.36
103601.11+084948.4	42.08±11.65	46.31±0.46	467.4±457.8	8.76±0.38

Table 5 continued

Table 5 *(continued)*

SDSS Name	T_{dust}[a]	$logL_{FIR}$[b]	SFR[c]	M_{Dust}[d]
J2000	K	erg/s	$M_{\odot}/yr$	$M_{\odot}$
113747.64+391941.5	37.92±6.55	46.33±0.42	487.1±319.9	9.03±0.34
114412.76+315800.8	43.63±4.98	46.68±0.34	1093.2±550.6	9.04±0.30
123132.37+013813.9	32.72±12.17	45.95±0.47	203.7±260.6	9.01±0.42
123743.08+630144.8	52.31±10.71	46.66±0.44	1036.3±758.1	8.57±0.38
132809.59+545452.7	30.99±2.03	46.44±0.15	626.1±183.6	9.63±0.15
133219.65+622715.9	37.71±5.13	46.44±0.38	634.2±375.9	9.15±0.31
142505.59+035336.2	31.62±3.64	46.26±0.34	413.6±210.5	9.40±0.32
144803.36+240704.2	47.81±18.41	46.29±0.49	441.3±532.9	8.42±0.42
150739.66-010911.0	31.54±2.316	46.65±0.23	1008.4±382.2	9.79±0.20
155203.30+352440.3	32.09±4.55	46.42±0.41	603.3±390.9	9.53±0.40
155645.30+380752.8	48.88±5.91	46.83±0.31	1526.1±735.7	8.91±0.28
160336.64+350824.2	52.94±4.71	47.11±0.26	2955.5±1220.7	9.00±0.22
163411.81+215325.0	43.08±8.65	46.66±0.45	1048.8±866.3	9.05±0.42
Control Sample 1	45.27±3.33	45.94±0.14	199.87±59.04	8.14± 0.14
Control Sample 2	48.64±5.68	46.10±0.30	287.22±138.0	8.17±8.12

[a] Dust temperature and its 1σ error is obtained from optimize fitting parameter. Initial fitting value is set to 45K and the range of temperature is set as 20K-65K

[b] FIR luminosity is calculated by integrating the rest frame flux density from 8μm to 1000μm

[c] SFR is estimated from FIR luminosity by applying Kennicutt Schmidt relation and we also make an assumption that 50% of total FIR luminosity will be contributed by AGN activity and the left will be heated by host galaxy star formation

[d] Dust mass is measured according to Berta et al. 2016 from the optimize fitting scale parameter by assuming an empirical opacity (Draine & Li 2001)

4. RESULTS

4.1. *Far Infrared SED*

According to photometry flux density measured in Section 3.4, we could know get rest frame FIR SED for each single WLQ target and our control sample. In addition, we also apply stacking analysis to WLQ a and WLQ b sample in order to compare WLQ dust emission with that of normal quasar directly from FIR SED. As is showed in Figure 6, we could see that rest frame flux density of normal quasar at all three SPIRE bands is significantly smaller than that of WLQ. When considering the average redshift of these two samples is almost the same, it indicates that the dust emission of WLQs is stronger than that of normal quasars. In the next several sections, we will try to use modified grey body dust model to fit with FIR SED and several parameters which is related to the properties of host galaxy star formation activities, including SFR, FIR luminosity, dust temperature and dust mass, to learn about conditions of star

formation heated Inter Stellar Medium (ISM) in WLQ host galaxies. However, there is a obvious discrepancy between optimize fitting dust model and WLQ stacking SED, which might be caused by limited size (not over 10) of WLQ sample. As a consequence, shape of WLQ stacking SED is distorted and could not be well fitted by our model, but for normal quasars, there are enough sources in each NQ sample (nearly 100), which is robust to get a physical stacking SED. So although the stacking SED of WLQs show an excess of FIR emission, we could not totally rely on this result. In the following, we will directly average parameters from FIR SED of each single WLQ target, but for our comparison sample, only stacking SED results can be obtained and is also reliable.

4.2. *FIR Luminosity and Star Formation Rate*

In Section 3.5, we have measured SFRs of all WLQ targets as well as our normal quasar comparison sample. Here, we could compare WLQ average SFRs with that of normal quasars. First of all, the av-
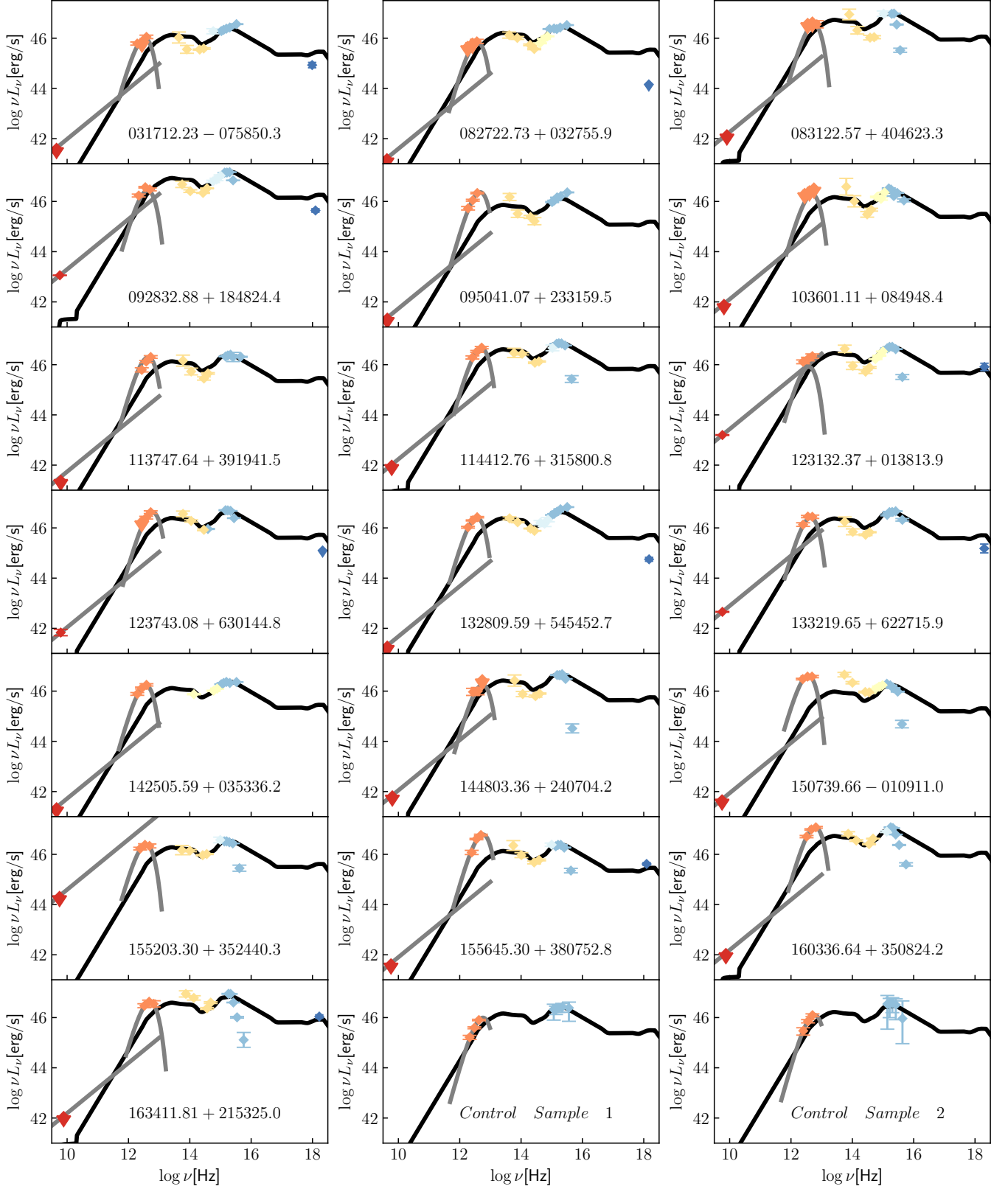
Figure 5. SED diagram of 19 WLQ targets and 2 control sample stacking results. For each panel above, from the left to the right, different color represent different sky survey data, including FIRST, SPIRE, WISE, UKIDSS/2MASS, SDSS, Chandra. The solid black line show the optimize fitting quasar template and the gray solid line show the radio continuum component and star formation heated cold dust emission component separately.
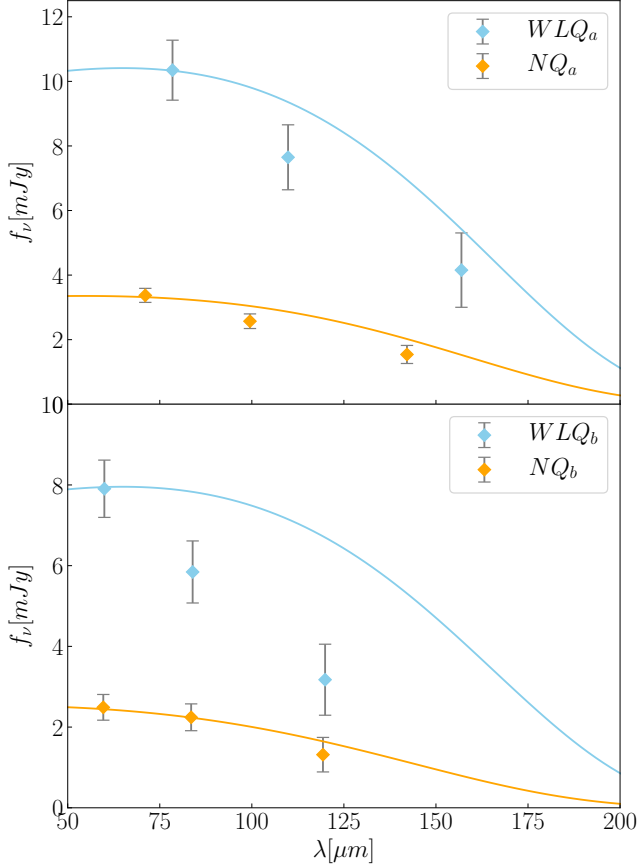
Figure 6. Stacking SED of WLQs and comparable normal quasars. Upper panel shows the stacking SED of WLQ_a and NQ_a. Lower panel shows the stacking SED of WLQ_b and NQ_b. The solid lines above show the optimize fitting modified grey body dust model

Figure 7. Star formation rates of WLQs and normal quasars. The first panel shows the SFR distribution of WLQ_a and NQ_a. The blue solid line represents mean level for WLQ_a and black solid line is for NQ_a stacking results. The second panel is the SFR distribution of WLQ_b and NQ_b. As is similar to first panel, blue solid line represents median level for WLQ_b and for NQ_a black solid line is stacking result. And for the third panel, it is for the WLQ_c SFR distribution Dashed lines in above three panels all represent 1σ confidence level.

erage SFRs estimated by comparison stacking analysis are $199.87 \pm 59.58 M_\odot/yr$ for NQ_a and $287.22 \pm 137.31 M_\odot/yr$ for NQ_b, corresponding to FIR luminosity of $8.88 \times 10^{(45)} erg/s$ and $1.27 \times 10^{(46)} erg/s$. However, as has been stated in Section 4.1, stacking analysis is not appropriate for WLQ targets. So here we apply the boot strapping method directly on the SFRs in WLQ_a, WLQ_b and WLQ_c samples. Eventually, average SFR of WLQ_a is about $407.85 \pm 135.80 M_\odot/yr$ at redshift of $2 < z < 2.5$ and for WLQ_b, it is about $1008.46 \pm 322.29 M_\odot/yr$ at redshift of $3 < z < 3.5$. As for WLQ_c, the average is about $955.68 \pm 622.76 M_\odot/yr$ and redshift range is $3.5 < z < 5.0$. The average FIR luminosity of these three samples are $1.81 \times 10^{46} erg/s$, $4.48 \times 10^{46} erg/s$ and $4.24 \times 10^{46} erg/s$ separately. All these results are showed in Figure 7 and dashed lines show 1σ confidence level. It obviously shows that star formation activity of WLQ is significantly strong so that the average median SFR of our WLQ targets are
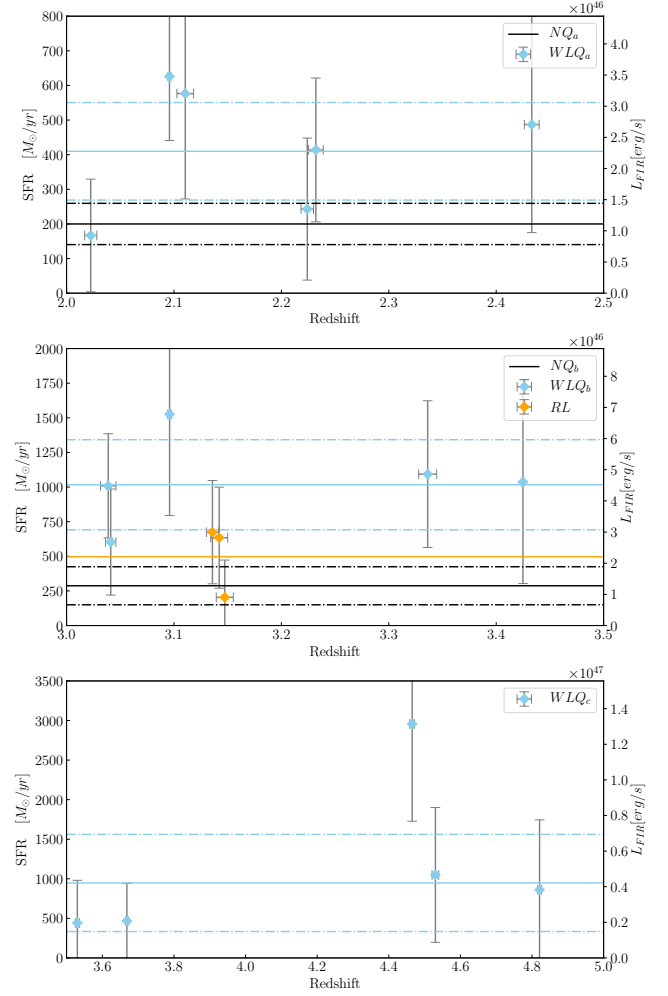
nearly twice that of comparison sample. The hypothesis test is applied and null hypothesis probability is about 4.28% at redshift $2 < z < 3.5$ and 4.89% at redshift $3 < z < 3.5$. In the analysis above, we have excluded three radio loud targets and all of three are in redshift range $3 < z < 3.5$. Here we also show them SFRs in Figure 6 which have been subtracted radio components when estimating SFRs and we can find that average SFRs of these radio loud targets are much lower than other radio quiet targets, indicating that their strong FIR emission is mainly contributed by radio jet com-

ponents instead of strong star formation activity. And for the other 5 WLQ targets at redshift of $3.5 < z < 5$, 3 of their SFRs are all over $900 M_\odot/yr$ and 2 targets even have SFRs over $1000 M_\odot/yr$, though with large uncertainty, which is still extremely strong star forming quasar host galaxy even in the whole quasar population. It indicates that at least for our radio quiet WLQ targets, their star formation activity is on average much stronger than that of SDSS normal radio quiet Herschel observed quasars with comparable luminosity and redshift. And about the interpretation on this result, we will discuss in Section 5.

4.3. Dust Mass

Apart from SFRs, all of our WLQ targets and normal quasar comparison sample have dust mass measurements and then another result is that dust mass of our WLQ sample is on average higher than that of SDSS normal radio quiet Herschel observed quasars with comparable luminosity and redshift, as is presented in Table 5 and Figure 8. For normal quasars, dust mass is nearly constant with $10^{8.14\pm0.15} M_\odot$ for NQ_a and $10^{8.12\pm0.26} M_\odot$ for NQ_b. However, dust mass of WLQs are about 1 factor higher, with $10^{9.17\pm0.25} M_\odot$ for WLQ_a and $10^{9.09\pm0.32} M_\odot$ for WLQ_b. The hypothesis test is applied and null hypothesis probability is about 3.28% at redshift $2 < z < 3.5$ and 3.89% at redshift $3 < z < 3.5$. In addition for WLQ_c, the average dust mass is about $10^{8.73\pm0.24} M_\odot$, which is still significant higher than normal quasar value. All of these is related to a extremely dust rich environment in WLQ host galaxy, which is also an indicator of a gas rich environment, which will be discussed in detail in Section 5.

4.4. Dust Temperature

In addition to SFR and dust mass, dust temperature is also an important parameter that describe properties of star formation heated dust in quasar host galaxy ISM. For normal quasars, average dust temperature similar to other typical quasar host galaxy dust temperature with $45.27 \pm 3.33K$ for NQ_a and $48.65 \pm 5.68K$ for NQ_b. However, for WLQs, the dust temperature is slightly lower than the values above with $33.35 \pm 3.09K$ for NQ_a and $41.06 \pm 6.37K$ for NQ_b. We also apply hypothesis test and confidence probability is 99.38% at redshift $2 < z < 3$ and 66.97% at redshift $3 < z < 4$. So at least for the WLQs at redshift of $2 < z < 3$, dust temperature of all the targets are lower than 40K with a median of 33K, which is rare in normal quasar with a typical temperature of 45K, but more similar to star-burst galaxies or Ultra Luminous InfraRed Galaxies (ULIRGs). But for WLQ_c at redshift $3.5 < z < 5.0$,
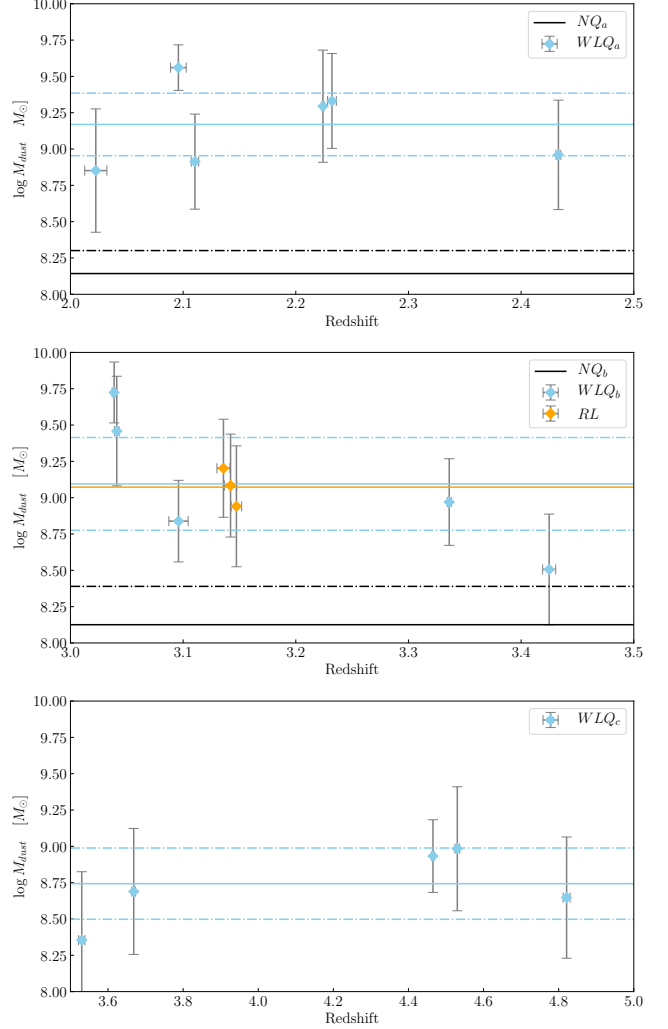

Figure 8. Dust mass of WLQs and normal quasars. The first panel shows the dust mass distribution of WLQ_a and NQ_a. The blue solid line represents mean level for WLQ_a and black solid line is for NQ_a stacking results. The second panel is the dust mass distribution of WLQ_b and NQ_b. As is similar to first panel, blue solid line represents median level for WLQ_b and for NQ_a black solid line is stacking result. And for the third panel, it is for the WLQ_c dust mass distribution Dashed lines in above three panels all represent 1σ confidence level.

average dust temperature is about 47.03 ± 6.41 which is almost common for dust in quasar host galaxies. So in some degree, this trend might be caused by the selection bias because WLQs with low temperature tends to have a higher flux density at SPIRE 250μm and 350μm band, then more possible selected by our sample selection criteria. Though it may not be a strong conclusion, it still indicates that chances are that there are more cold gas and dust in WLQ host galaxies. Yet this argument should require more observation tests.
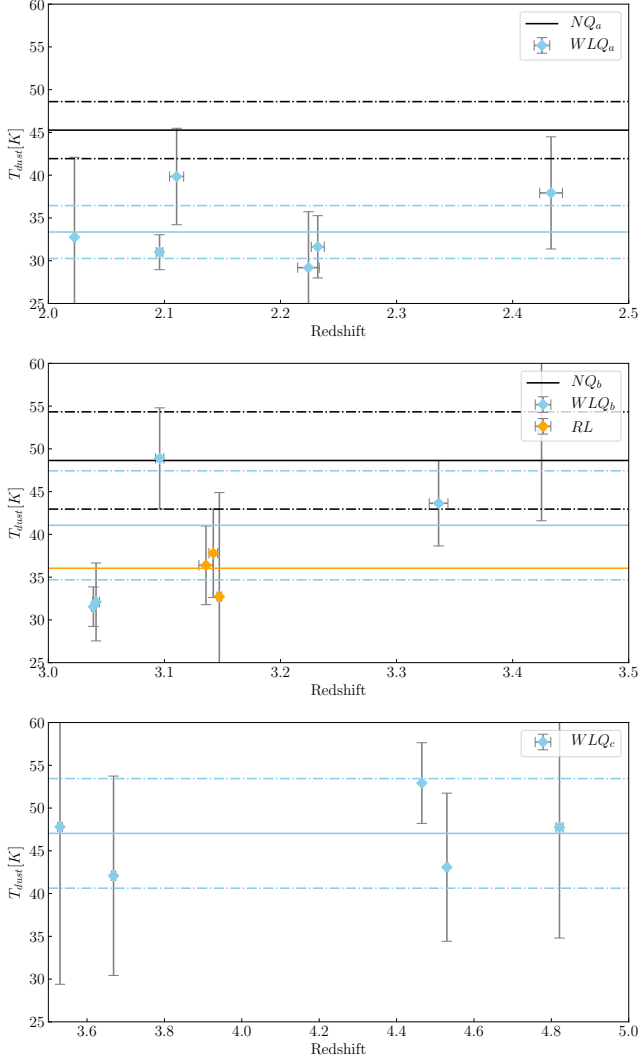
Figure 9. Dust temperature of WLQs and normal quasars. The first panel shows the dust mass distribution of WLQ_a and NQ_a. The blue solid line represents mean level for WLQ_a and black solid line is for NQ_a stacking results. The second panel is the dust temperature distribution of WLQ_b and NQ_b. As is similar to first panel, blue solid line represents median level for WLQ_b and for NQ_a black solid line is stacking result. And for the third panel, it is for the WLQ_c dust temperature distribution Dashed lines in above three panels all represent 1σ confidence level.

5. DISCUSSION

5.1. *Theories of WLQs*

It has been puzzling to explain the origin of weak line features of WLQs and there are two major scenario when considering the photo-ionization model: one is caused by the lack of high energy photon to ionize gas in BELR due to soft ionization continuum and the other is BELR scenario mainly focus on special properties of gas content in BELR.

For the soft ionization continuum SED theory, it is possible for several mechanisms to produce soft continuum prior to illuminating BELR. First to all, temperature of a standard thin accretion disk with a black hole mass higher than $3.6 \times 10^9 M_\odot$ under non spinning condition will be too low to photo-ionize the BELR (Laor Davis et al. 2011). But near infrared (NIR) spectroscopy study on WLQs shows that the EW of high ionization emission line will be relatively lower than low ionization line (Plotkin et al. 2015), which contradicts cold accretion disk hypothesis that all of the emission line should be weak in the same way. Also there are still many WLQs with black hole mass lower than $10^9 M_\odot$ which is hard to interpret under this explanation. Apart from low photon temperature, super Eddington accretion could also account for this, as has been proposed in PHL 1811 (Leighly et al. 2007a; 2007b). However, result on WLQs X-ray observation and optical to NIR spectroscopy found that the accretion rate of WLQs are typical of ordinary quasars with similar redshift and luminosity (Shemmer et al. 2009, Shemmer et al. 2015), indicating that WLQs are not likely to be extremely high accretion rates system.

In addition, orientation effects under shielding-gas scenario could possibly unify the X-ray weak and X-ray normal WLQ populations (Jianfeng Wu et al. 2011; Bin Luo et al. 2015). The shielding gas might naturally be understood as a geometrically thick inner accretion disk which shields the broad line region from the ionizing continuum when the inner disk was puffed up under the condition $\frac{L}{L_{Edd}} \gtrsim 0.3$. Under this situation, we will observe a weak X-ray WLQ if there is shielding gas on our line of sight and on the other hand, a X-ray normal quasar will be observed at lower inclinations without high ionization shielding gas absorption. And for WLQs with low Eddington ratios, standard thin disk system will not produce such like "shielding gas" to absorb X-ray radiation so that X-ray normal quasar will be observed. And more, the discrepancy between high and low ionization emission line could also be partly explained by difference of power and pressure of high energy photon due to "shielding gas" absorption. Till now, it is still an possible interpretation but lack of strong evidence.

As for anemic BELR scenarios, low gas content or low covering factor of WLQs could be the possible explanation (Shemmer et al. 2010, Nikolajuk Walter et al. 2012). Nevertheless it still cant interpret the difference between low and high ionization emission line. Another possible interpretation is the structure of BELR of WLQs hasn't been fully formed when they are observed
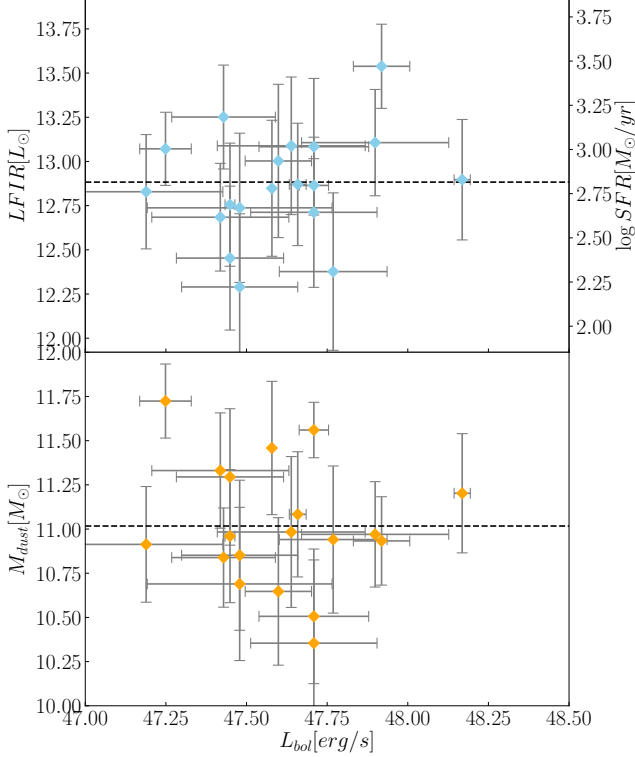
Figure 10. Relations between bolometric luminosity and FIR luminosity and host galaxy gas mass. The upper panel shows the relation between FIR luminosity and bolometric luminosity and the lower panel shows the relation between host galaxy gas mass and bolometric luminosity. The dashed line shows average value and error bar represents $1\sigma c$ confidence level

(Hryniewicz et al. 2010). The formation of BELR and NELR should need disk wind carry material and move out of the accretion disk to make up gas content of BELR. Under this scenario, low ionization emission line like MgII will be formed prior to high ionization emission line like CIV because of different distances to disk of their formation regions. It is plausible to explain properties of emission lines and broad band UV-optical SED but hard to account for X-ray weak WLQs. However, this scenarios because that WLQs are just at an early stage of quasar and a disk wind is freshly launched so the low ionization lines formed close to the disk surface will be observed but with relatively low EW and strong blue shift. However high ionization lines or narrow line will only be viewed until the wind reaches BELR further from disk surface.

5.2. Merger Driven Starburst Host Galaxy

First of all, average SFRs for WLQ_b and WLQ_c are nearly $1000 M_\odot/yr$, indicating many of these WLQs are

quasar-starburst systems. Even for WLQ_a, its median SFR is also much higher than NQ_a value on average. Results of SFRs shows that WLQs have much stronger star formation activity than that of normal quasars with comparable luminosity and redshift, suggesting a recent starburst so that strong star forming is still ongoing. In addition, all of our WLQ sample have a strong FIR luminosity over of $10^{12} L_\odot$, with an average of $10^{12.88} L_\odot$, which could be classified as ULIRGs and there are also 6 targets that have FIR luminosity over $10^{13} L_\odot$ and could be identified as Hyper Luminous InfraRed Galaxies (HLIRGs). Both ULIRGs and HLIRGs suggest that the host galaxy is during the star burst stage triggered by major merger. Secondly, a extremely high dust mass is also an indicator of gas fuel environment. Here using an empirical dust to gas ratio in the Milky Way, we estimated WLQ host galaxy gas mass and plot them verse bolometric luminosity in Figure 10. It shows that average gas mass of WLQs are about $10^{11} M_\odot$, which could be caused by extremely gas rich quasar host galaxy or a actual higher dust to gas ratio, suggesting that ISM in WLQ host galaxies either have higher than other gas fuel for star formation and black hole accretion or have more fraction dust content. Both of them are consistent with merger star burst galaxy scenario. Thirdly, relatively lower dust temperature of WLQs, especially at redshift $2 < z < 3$, also conform to the point that there are copious cold gas fuel in quasar host galaxy. Considering all the properties of WLQs, especially our Herschel FIR study and previous multiwavlength research, we propose that WLQ is one kind of early type quasar whose host galaxy has gone through a recent starburst caused by the major merger.

5.3. Early Stage Of Quasar Evolution

Here, we will start from the point that AGN activities of WLQs are triggered after host galaxy major merger to make an attempt to interpret the physical origin of its strange properties. As has been stated above, WLQs are post merger quasar-starburst system in which there are large amount of gas fuel both for star formation and central SMBH accretion. After the central binary SMBH merger and began to form accretion disk, the high energy radiation will be generated and photon pressure will push central dust grains away to form dust torus and heat it. Under this situation, the broad band UV-optical-MIR SED will became similar to normal radio quasar if radio jet isn't on line of sight. And at the same time, host galaxy star burst is still ongoing, so we will find star formation heated dust emission of WLQs is stronger than that of normal quasars with similar redshift and luminosity.

However, because of this early stage of WLQ in quasar evolution, other structure of quasar has remained nor fully constructed, like BELR and Narrow Emission Line Region, which belongs to what we refer as one mechanism of anemic BELR scenario. As has been discussed in literature, the formation of BELR and NELR requires the disk wind to carry the ionized matter to construct line region structure. And during the time before BELR or NELR fully formed, we will see extremely weak broad emission line or narrow emission line because of the lack of related gas content. In this way, the most marked characteristic, weak emission line could be naturally interpreted without involving complex physical mechanism related to the accretion disk. Further more, in fact it will take quite a lone time to form the complete structure of BELR, so the region near the disk where low ionization emission lines like MgII are primarily generated will be finished earlier. On the other hand, high ionization emission line and narrow emission line will require more time. Under this situation, the observational fact that there is a discrepancy between the EW of high and low ionization emission line, like CIV and MgII could also be explained by the evolution delay between their relevant structure. Actually, it will also be straightforward to understand why there is often a strong disk dominated blueshift component in CIV of WLQs, sometimes even in MgII, which is hard to be explained by the soft continuum scenario like extremely cold photon temperature caused by the SMBH and even accretion disk "shielding gas".

Although we tend to regard not fully formed BELR as major mechanism for WLQ, nevertheless, we could not rule out all other physical mechanism in accretion disk that might also contributed to properties of WLQ only from our FIR study results. Apart from that, it remains puzzling that there are two categories of WLQs, X-ray normal and X-ray weak. A possible explanation is that there is a "shielding gas" caused by the high accretion rate slim thick disk which absorb the high energy photon in the line of sight of observer. But the reason why there is a significantly fraction of such a high accretion rate system has not been figured out. Here in post merger early type quasar scenario, there is abundant gas fuel for the growth of central newly formed SMBH, which tends to form a high accretion rate disk system, super Eddington for example and then generate the X-ray weak WLQs because of the "shielding gas" absorption. Our WLQ sample is one case for WLQs with high accretion rates. However, if there is no "shielding gas" on our line of sight or strong accretion activity has be stopped when there is not enough gas fuel then we will observe a X-ray normal WLQ. In addition, there are still several

limitations on our study. Firstly, according to the Figure 1 in Section 3.1, our sample only involves extremely high luminous WLQs with bolometric luminosity over $10^{47} erg/s$ and majority of them is around Eddington limit. Though lots of WLQs are relatively luminous, it still requires us to conduct more study on less luminous targets and it will remain a question if their SFRs will be significant higher than normal quasar with comparable redshift and luminosity. Apart from this, many WLQs actually are the normal accretion rate system which are below Eddington limit and in these systems, it remains a question that if they are post merger quasar-starburst system and the star formation activity should be studied in detail, which is important for us to further understand intrinsic properties of WLQ. And more X-ray studies on WLQs are still required because our sample sample size, only two identified X-ray weak targets, limit us to have complete X-ray research in order to test our hypothesis on the X-ray radiation. More and more multiwavelength observations especially at FIR/sub-millimeter and X-ray are needed to have a deep insight into the WLQs, which is essential for us to understand the evolution sequence of quasars and their host galaxies.

6. SUMMARY AND CONCLUSION

We have Herschel SPIRE photometry observation on 19 high redshift WLQs at $2 < z < 5$ selected from previous literature with reliable redshift estimate and no $Ly\alpha$ absorption features. Standard HIPE point photometry pipeline is applied to all bands high sensitivity image of individual target. Before that, radio component has been subtracted by a model PSF based on a flat radio continuum with an assuming spectral index of 0. Other multiwavelength data from X-ray to MIR is obtained from literature or archive in order to have a good inspection on sample properties. Dust model fitting is conducted to the FIR flux density by Python Curve-Fit program. SFRs are all measured by the far infrared luminosity which is calculated from the integration of the optimize fitting gray body dust model. In addition, a comparison sample is selected from normal radio quiet SDSS quasar which has SPIRE image data from HHLI and comparable redshift and luminosity range. The average median SFR of comparison sample is estimated from average SED generated by stacking analysis but for the WLQ targets, we directly use boot strapping method to each individual SFR. Final results show that our radio quiet WLQ sample have a strong star formation activity on average that of normal quasar. When considering previous multiwavelength work, we finally conclude that WLQs are one kind of early type quasar whose host galaxy has just gone through starburst stage

so that there is still continuing strong star formation activity. While the central AGN is just at the early evolution stage where BELR and NELR has not been completely formed which accounts for the weak emission line features of WLQs. However, there remains several puzzles because of the limitations of our study, which requires more and more future research on this kind of special quasars and reveals the intrinsic origin of WLQs.